ACHIEVING HOT-DAY TAKE-OFF WITH FUEL CELLS THROUGH EFFICIENT THERMAL MANAGEMENT

L. Braumann*, C. Gross*, A. Juen*, H. Amri*
*Advanced Drivetrain Technologies GmbH, Leonard-Bernstein Straße 8/2/EG01, 1220 Wien, Österreich

Summary

This paper outlines the preliminary design process of the thermal management system in exFan. Results for mass and energy consumption of three concepts to increase heat quality are presented: (1) LT-PEMFC with a heat pump for the battery cooling circuit to allow heat rejection during high ambient temperatures (2) both LT-PEMFC and battery coolant circuit with a heat pump to increase the heat quality of the largest heat sources up to 240°C and (3) HT-PEMFC with an operating temperature of up to 160°C. The investigation is performed for different power splits of fuel cell and battery with the goal to provide the possibility of hot-day take-off for fuel cell electric aircraft. This research builds on the findings of Link et al. 2023 and Kellermann et al. 2022. The results outline that a VCS heat pump with a condenser-temperature of 160°C provides a mass reduction of approx. 14% to the TMS. The application of a HT-PEMFC even reduces the TMS mass by 65%.

1. INTRODUCTION

Hydrogen fuel cell powered aircraft propulsion is one key technology to enable environmentally friendly aviation. Electrically driven and fuel cell powered propulsion systems enable zero in-flight CO2 emissions. One of the main challenges of fuel cell powered aviation is thermal management and heat rejection. Electrical efficiencies of fuel cells are predicted to reach 50% by 2030. This means each Watt of electricity produced in the fuel cell will generate a Watt of heat that needs to be dissipated. While combustion engines can reject the majority of waste heat through exhaust gases, the heat produced by a fuel cell has to be dissipated via a heat exchanger. The resulting excessive size and air resistance of heat exchangers is a showstopper for hydrogen-electric aircraft. The Horizon Europe project exFan (101138184) solves this problem by innovating a fuel cell electric aircraft thermal management and recuperation system: The exFan propulsion system applies the Meredith-Effect to produce thrust from waste heat. This has the potential to increase the thermal efficiency of the propulsion system by 8% compared to heat dissipation via a surface heat exchanger that does not add drag. Optimized additively manufactured heat exchangers (HX), novel surface technologies to inhibit fouling of the HX, a thermal management concept that increases the temperature difference as well as highly efficient geared drivetrain configurations are developed to TRL3 to achieve a compact MW-class propulsion system for future fuel cell electric aircraft. The thermal management system for a fuel cell electric propulsion system has to control the temperature of components with different operating temperatures: Li-Ion batteries can operate at up to 45°C, PEM-fuel cells (PEMFC) at up to 80°C with the gearbox, power electronics and electric machine being able to run at slightly higher temperatures. Due to the low temperature of the heat sources, heat dissipation during take-off on hot days with over 40°C on the ground is a major challenge for fuel cell electric aircraft. If a standard configuration of coolant pumps and heat exchangers is used, the thermal management system (TMS) will become vastly oversized only to be able to take off during hot days. A more sophisticated approach is necessary in order to make fuel cell electric aircraft a feasible and competitive solution for climate neutral aviation.

2. STATE OF THE ART OF ELECTRIC AIRCRAFT THERMAL MANAGEMENT

Vapor-cycle machines (VCM) consist of a condenser, a mechanical pump, an evaporator and an expansion valve. Within this mechanism, two-phase refrigerant is cycled. These mechanisms are regularly used for industrial refrigeration and are applied to aircraft for air conditioning purposes (e.g. Embraer Phenom 100 & 300).[1] VCM are also additionally purposed for cooling of avionics and batteries, such as the MicroVCS by Honeywell, which is featured in the F22 Raptor, F 16 Fighting Falcon, F/A 18 Super Hornet and used in the Archer Midnight.[2] [3] The MicroVCS was also announced to cool the batteries of the LiliumJet.[4] Thus, the TRL of VCMs can generally be considered high. However, applications of VCM for future fuel cell electric aircraft, that need to handle multiple MW of heat have yet to be tested in a laboratory setting (<TRL4). Also for these applications, VCM may be a feasible solution to increase the heat quality.[5] Kösters et al.[6] reviewed the use of a VCM using water as working fluid. They used the VCM to cool an LT-PEMFC and keeping the heat exchanger surface small by raising the temperature from 56.4°C (coolant) to 324.4°C (working fluid at condenser). The application of the ramjet effect allowed to reduce the effective drag due to the heat exchanger by 96.8% and saved about 16% net propulsion thrust. While drag was the figure of merit for Köster et al., it was not outlined how the mass of the compressor of the VCM was defined. For turbofan engine oil cooling, investigations by Maalouf et al.[7] have shown that VCM are not beneficial for their defined use case, but are a promising solution for engines with lower coolant temperatures and high heat loads – both of which are present in fuel cell electric aircraft. Common working fluids are R22, R134a and R410a, but their use depends strongly on the application.[8]

Another promising heat pump technology is the thermoelectric heat pump. This technology uses the Peltier effect to generate a temperature difference using electric

power. The relation between the required electric power and the cooling power, however, is generally worse than with VCMs. Still, the Peltier effect coolers have some remarkable attributes which make them useful as heat pumps in aviation applications: No moving parts/fluids are necessary, the TEC is insensitive to movement and its performance is almost independent of its capacity. Additionally, peltier devices can react readily to changing operating conditions.[9] Kellermann et al.[10] investigated the use of peltier effect heat pumps for a 19-seat hybrid electric aircraft with positive results.

NASA has performed investigations on a heat pump based on energy transport with acoustic waves. This acoustic heat pump uses aircraft engine waste heat to produce a high intensity acoustic wave. The associated thermal management system extracts high-exergy waste heat from a combustion engine and converts the heat into a traveling acoustic wave that may act as a heat pump for low thermal quality heat sources.[11] While this heat pump system may have remarkable benefits for hybrid-electric systems, it is not applicable to a full electric aircraft within the scope of this research.

The fuel cell is the main source of heat in a fuel cell electric aircraft due to its efficiency, which may improve from the 2020 state of the art of 43.5% to 50% by 2030 according to the KPIs of the Clean Hydrogen Joint Undertaking (CHJU).[12] A review by the DLR compares fuel cells for aviation aircraft: Currently, low-temperature proton exchange membrane fuel cells (LT-PEMFC) have the highest TRL and performance. Such FC provide 840mW/cm2 at a commercial level and run at temperatures around 60-90°C. The combination of large amounts of generated heat with a low heat quality has a negative impact on the aircraft thermal management system. LT-PEMFC are used in the 19-seat Dornier 228 test aircraft of ZeroAvia, the Universal Hydrogen ATR 72 retrofit and the H2Fly 4-seater aircraft. High-temperature PEMFC (HT-PEMFC) have a medium TRL[13] and run at higher temperatures around 120-180°C. Considering an ambient temperature of 43.3°C on a hot-day during take-off, this means that the temperature difference between coolant and ambient air is at least 2 times higher when using a HT-PEMFC. Applying Newton's law of cooling, this roughly translates to a reduction of the required heat exchanger surface by half. Due to the large expected benefits, ZeroAvia[14] is developing HT-PEMFC and research projects such as NIMPHEA[15] investigate high-temperature membrane electrode assemblies that operate at 120°C and have a power density of 1.25W/cm2 – surpassing the power density of LT-PEMFC while providing higher operating temperatures. Finally, solid oxide fuel cells (SOFC) are another feasible fuel cell type that can reduce the TMS mass due to their high operating temperature beyond 600°C. SOFC are considered to be at medium TRL for aviation applications.[13] Projects such as FlyEco[16] aim at integrating SOFC in future hybrid-electric aircraft.

3. RESEARCH QUESTION

This research aims to answer the following research questions:

(1) Can heat pumps based on the vapour cycle or TEC significantly decrease the TMS mass of a fuel cell aircraft during hot-day take off?

(2) Will heat pumps be an alternative to HT-PEMFC development for future fuel cell aircraft?

4. METHOD

To investigate the behaviour of the thermal management system (TMS), its components are modelled to derive mass and power consumption. The modelling methodology is described below. Validation results of new or differently applied models are shown in appendix-A.

4.1. Modelling approach

The modelling is performed for a simplified TMS that only considers the energy system consisting of fuel cell and battery as heat sources. Other downstream sources of low-quality heat that have lower impact on the TMS sizing such as inverters, electric motors, gearboxes and the TMS for the hydrogen fuel system are not considered. The TMS investigated here consist of a combination of the following components: pumps, pipes, coolant, refrigerant, heat exchangers and heat pumps. The following section outlines the three investigated architectures.

4.1.1. Investigated Architectures

Figure 1 shows Architecture 1 (A1) of the thermal management system for LT-PEMFC and batteries. A1 consists of a HX, a coolant pump that transports a liquid water-glycol coolant to a battery and a fuel cell in series. The battery is connected through a TEC-system to the coolant circuit, that raises the heat quality of the battery from 30°C to 80°C. The LT-PEMFC is considered to operate at 80°C. The heat exchanger is of the plate-fin type.

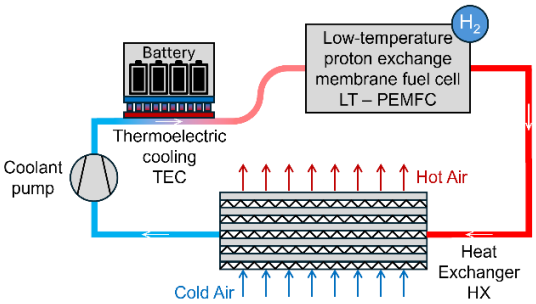

Figure 1: Architecture I (A1): Conventional cooling cycle using a TEC module for the battery.

Figure 2 shows the Architecture 2 (A2). In comparison to A1, an additional heat pump system is added, which uses water as a refrigerant. The heat pump system is made up of an evaporator, a compressor, a condenser and an expansion valve. The heat pump raises the temperature level of the TMS from 80°C to 120-240°C. Both evaporator and condenser are considered as plate-fin HX. The compressor is a screw compressor. Recuperation at expansion is not considered.

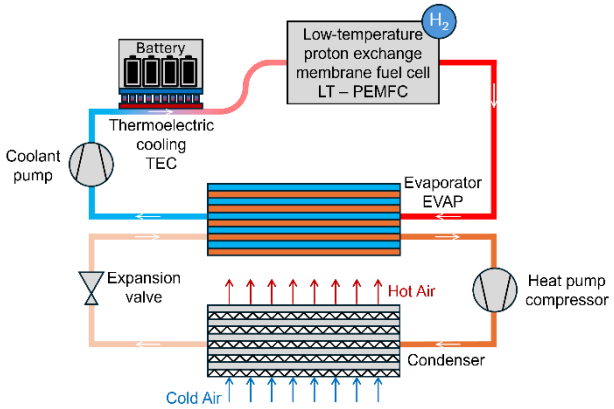

Figure 2: Architecture 2 (A2): Cooling cycle with heat pump

The third Architecture consist of two separate coolant cycles and is depicted in Figure 3. The left cooling cycle controls the temperature of the battery with a TEC. The right cycle cools a HT-PEMFC. A dedicated heat pump is not necessary, due to the high operating temperature of the fuel cell.

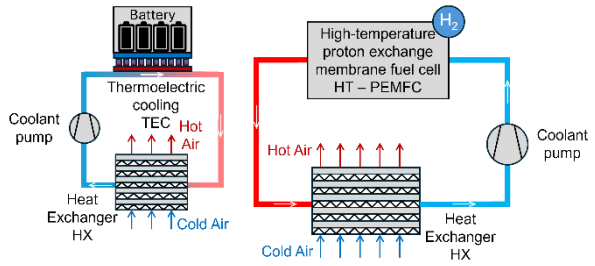

Figure 3: Architecture 3 (A3): Cooling cycle for HT-PEMFC

4.1.2. Assumptions on heat sources

In order to consider the effect of the power-split ratio, the fuel cell and battery have to be sized accordingly. This sizing process is performed for a year 2030+ aircraft with the following performance parameters shown in Table 1. If there exist predictions for future performance, the chosen values are underlined.

Table 1: Heat Sources

Battery Type	**2040+ LiS Battery**	**Source**
Power Density Pack	500 W/kg @1C	[18]
Energy Density Pack	550 Wh/kg	[18]
Energy Efficiency	85%	[18]
Operating temperature	30°C	assumed

Fuel Cell Type	**LT-PEMFC**	**Source**
Power Density stack.[1] + air supply	3.5/4.5/5.5 kW/kg (2026/30/35)	[19]
Operating Temperature	80/90/100 °C (2026/30/35)	[19]
Efficiency at nominal power	50%	[12]

Fuel Cell Type	**HT-PEMFC**	**Source**
Power Density stack + air supply	1.5/2.5 kW/kg (2030/35)	[19]
Operating Temperature	120/160 °C (2030/35)	[19]
Efficiency at nominal power	55%	[20]

4.1.3. Aircraft boundary & airside operating conditions

Take-off and climb are the flight phases which have the most impact on the TMS sizing. This is due to the combination of high power demand and high ambient temperatures, which can reach up to 43.3°C in the European climate zone.[17] The International Standard Atmosphere (ISA) model has a sea level reference temperature of 15°C. Thus 43.3°C are assumed as the ambient temperature for hot-day take-off. The boundary conditions are depicted in Table 2.

Table 2: Boundary Conditions

Aircraft propulsion system shaft power	1MW	assumed
Air velocity at T/O	275km/h	similar to A320
Ambient Temperature	43.3°C	MIL-HDBK-310

4.2. Models

4.2.1. Pipes & Pumps

The mass estimation of pumps and coolant is taken from Link and Staggat[21].

[1] The authors conclude from BOP mass results in [19], that the power density of the stack + air supply is approximately half the stack power density.

Coolant pump

The coolant pump power is estimated via eq. (1).

$$P_{pump} = \frac{\dot{V}_h \cdot \Delta p_{pipe}}{\eta_{pump}} \quad (1)$$

$$m_{pump} = 3294.1 \cdot \dot{V}_h + 3.094$$

P_{pump} … power of coolant pump in W
$\dot{V}_h$ … volume flow in m³
Δp_{pipe} … pressure loss over pipe in Pa
η_{pump} … pump efficiency
m_{pump} … pump mass in kg

Coolant mass

The coolant mass estimation in eq. (2) is based on the circulation time of the coolant through the coolant circuit.

$$m_{Coolant} = \dot{m}_h \cdot \Delta t_{Circulation} \quad (2)$$

$m_{Coolant}$ … coolant mass in kg
$\dot{m}_h$ … coolant mass flow in kg/s
$\Delta t_{Circulation}$ … circulation time in s

Pipe mass

The flow area of the coolant circuit pipes is calculated via the coolant mass flow rate and an assumed coolant flow speed of 1 m/s. The inner pipe diameters is calculated from the flow area. The thickness of the aluminium pipe is assumed to be 2 mm. The piping mass can then be calculated with eq. (3):

$$m_{Pipe} = \frac{\pi}{4} \cdot \left(d_{PipeO}^2 - d_{PipeI}^2\right) \cdot l_{Pipe} \cdot \rho_{Pipe} \quad (3)$$

m_{Pipe} … pipe mass in kg
$d_{pipeI,O}$ … pipe diameter in m
l_{pipe} … pipe length in m
ρ_{pipe} … pipe density in kg/m³

For the calculation of the coolant pump, the pressure losses in the coolant pipes are calculated with the Darcy Weisbach equation.

4.2.2. Heat Exchangers

For the estimation of mass, dimensions and pressure drop in the heat exchanger, a Rectangular Offset Strip Fin (ROSF) heat exchanger was chosen. The model is based on Bachmann et al.[22] and the compact heat exchanger reference by Shah et al.[23] Since these correlations are mainly valid for low Reynolds numbers, a model validation was performed by comparing the model to experimental results by Saltzman et al.[24] in Annex A. The method developed by Bachmann is based on non-dimensional geometry parameters which describe the geometry of a heat exchanger cell. For each of these heat exchanger cells, the hydraulic diameter and the Reynolds number are calculated. This is used to calculate the Colburn factor j and the Fanning friction factor f. These factors and the heat transfer area A_{Cell} are used to calculate the heat transfer coefficient h of a heat exchanger cell.

$$Nu = j \cdot Re \cdot Pr^{\frac{1}{3}} \quad (4)$$

$$h = \frac{Nu \cdot k_{Fluid}}{D_h} \quad (5)$$

N_u … Nusselt number
j … Colburn factor
Re … Reynolds number
Pr … Prandtl number
h … heat transfer coefficient in W/(m²K)
k_{fluid} … thermal conductivity in W/(mK)
D_h … hydraulic diameter in m

The heat transfer coefficient U times the total surface area A of a heat exchanger cell is calculated in eq. (6) as follows (subscripts h and c stand for hot and cold fluid):

$$(U \cdot A)_{cell} = \frac{1}{1/(h \cdot A_{cell})_h + 1/(h \cdot A_{cell})_c} \quad (6)$$

U … heat transfer coefficient
A … total surface area of HX cell

Differing with Bachmann's approach, the heat exchanger is made up of multiple slices, one cell wide each as can be seen in Figure 4. Consequently, it can also be used for two-phase fluids. The hot fluid (refrigerant) flows from each slice to the next and the enthalpy of the exiting fluid is the input for the next HX slice. The cold fluid (Air) flows perpendicular to the hot fluid flow and gets heated up, while removing heat from the hot fluid.

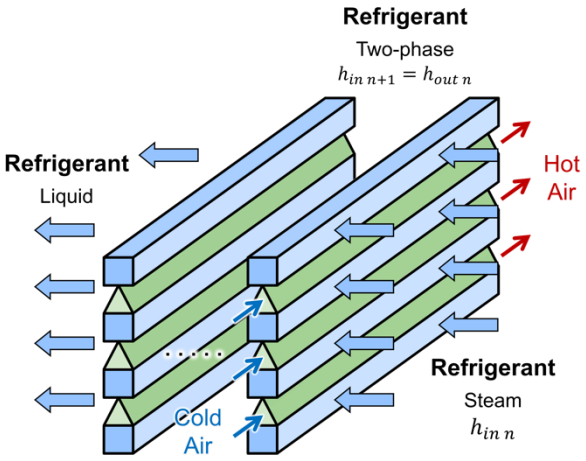

Figure 4: heat exchanger model

For each of the one cell wide HX slices the heat exchanger effectiveness is calculated via the ε – NTU method. To use this the heat capacity for both mass flows have to be calculated via eq. (7).

$$\dot{C} = \dot{m} \cdot c_P \quad (7)$$

$\dot{C}$ … heat capacity flow rate in J/(K s)
$\dot{m}$ … fluid mass flow in kg/s
c_P … specific heat capacity in J/(kg K)

The smaller heat capacity flow gets the index "min" and the larger one the index "max". Then the ratio $C^* = \dot{C}_{min}/\dot{C}_{max}$ is calculated. The number of heat transfer units are evaluated by the following equation (8):

(8) $$NTU = \frac{U \cdot A}{\dot{C}_{min}}$$

NTU … number of transfer units

Now the heat exchanger effectiveness is calculated in eq. (9) with the values of NTU and C^* based on the equation from Table 3.3 on page 117 in Fundamentals of heat exchanger design [23]

(9) $$\begin{aligned} \varepsilon &= 1 - \exp(-\mathrm{NTU}) \\ &\quad - \exp[-(1+C^*)\mathrm{NTU}] \sum_{n=1}^{\infty} C^{*n} P_n(\mathrm{NTU}) \\ p_n(y) &= \frac{1}{(n+1)!} \sum_{j=1}^{n} \frac{(n+1-j)}{j!} y^{n+j} \end{aligned}$$

ε … heat exchanger effectiveness

With this the heat transfer rate of each slice can be calculated with eq. (10):

(10) $$q = \dot{C}_{min} \cdot (T_{h,i} \cdot T_{c,i}) \cdot \varepsilon$$

q … heat transfer rate in W

The hot fluid enthalpy at the outlet of each slice is given in eq. (11):

(11) $$h_{hO} = h_{hI} - \frac{q}{\dot{m}_h}$$

$h_{hI,O}$ … enthalpy at inlet and outlet in J

Heat exchanger slices are added until the hot fluid outlet temperature of the last slice is less than the set limit.

The model can be used for single phase heat exchangers as well as two phase heat exchangers. In two-phase heat exchangers the hot fluid (refrigerant) enters as superheated steam and exits as subcooled liquid, as can be seen in Figure 5.

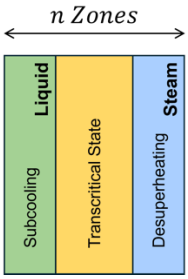

Figure 5: two-phase heat exchanger

Both of the heat exchangers shown in Figure 6 are calculated with the same HX model. In the two-phase heat exchanger, the heat is expelled to change the phase from steam to liquid, while in the single-phase heat exchanger the temperature of the hot fluid drops.

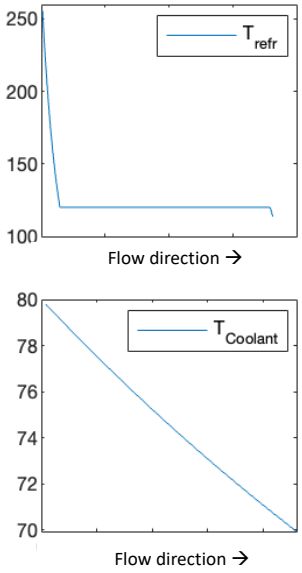

Figure 6: Two-phase (top) vs one-phase HX (bottom)

4.2.3. Thermoelectric Cooling

The heat flux on the cold and hot side and the electrical power for the TEC are calculated using the improved simplified model from the research of G. Fraisse [25]. Compared to the simplified standard model, a significant improvement in the accuracy of the model can be achieved by taking the Thomson effect into account.

The heat flux for the hot side was calculated according to the following eq. (12).

(12) $$Q_H = \alpha_H \cdot I \cdot T_H - \bar{K} \cdot \Delta T + \frac{1}{2} \cdot \bar{R} \cdot I^2 - \frac{1}{2} \cdot \bar{\tau} \cdot I \cdot \Delta T$$

Q_H … Heat flux for the hot side in W
α_H … Seebeck coefficient for the hot side (V/K)
I … Electrical current in A
T_H … Temperature on the hot side in K
$\bar{K}$ … Thermal conductance at mean temperature in W/K
ΔT … Temperature difference between c. and h. side in K
$\bar{R}$ … Electrical resistance in Ω
$\bar{\tau}$ … Thomson coefficient at mean temperature in V/K

For the heat flux on the cold side eq. (13) is used.

(13) $$Q_C = \alpha_C \cdot I \cdot T_C - \bar{K} \cdot \Delta T - \frac{1}{2} \cdot \bar{R} \cdot I^2 + \frac{1}{2} \cdot \bar{\tau} \cdot I \cdot \Delta T$$

Q_C … Heat flux for the cold side in W
α_C … Seebeck coefficient for the cold side (V/K)
T_C … Temperature on the cold side in K

The electrical power required corresponds to the difference between these two heat fluxes. This results in the electrical power in eq. (14).

(14) $$P = (\alpha_H \cdot T_H - \alpha_C \cdot T_C) \cdot I + \cdot \bar{R} \cdot I^2 - \bar{\tau} \cdot I \cdot \Delta T$$

P … Electrical power in W

The coefficient of performance (COP) in TEC mode is

therefore calculated via eq. (15).

$$COP_c = \frac{Q_C}{P} \tag{15}$$

COP_c … Coefficient of performance in –

The area, leg length and density of the material are required to calculate the mass of the TEC. The mass of the TEC is therefore calculated in eq. (16).

$$m_{TEC} = m_{Leg} + 2 \cdot m_{Plate} = A_{Leg} \cdot l_{Leg} \cdot \rho_{Leg} + 2 \cdot A_{Plate} \cdot l_{Plate} \cdot \rho_{Plate} \tag{16}$$

m_{TEC} … Mass of the TEC in kg
m_{Leg} … Mass of the thermoelectric element in kg
m_{Plate} … Mass of the interconnect plates in kg
A_{Leg} … Area of the thermoelectric element in m²
l_{Leg} … Length of the thermoelectric element in m
ρ_{Leg} … Density of the thermoelectric element in kg/m³
A_{Plate} … Area of the interconnect plates in m²
l_{Plate} … Thickness of the interconnect plates in m
ρ_{Plate} … Density of the interconnect plates in kg/m³

For the following investigations definitions of the mass and required electrical power of the TEC were defined. An input temperature of 30°C on the cold side and an output temperature of 80°C on the hot side were chosen. This corresponds to a temperature difference of 50°C.

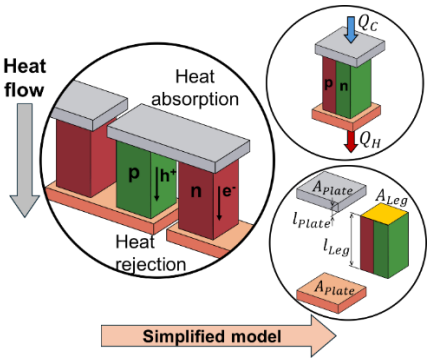

Figure 7: TEC Model

4.2.4. Compressor Modeling

For the heat pump compressor, a screw compressor was chosen due to the compatibility of these compressor types with water vapor as a refrigerant.[25] Screw compressors have also been used for aerospace sector heat pump systems.[26] This research uses a simplified method to calculate the mass and required power of the screw compressor based on Royce et al[27]. Tables for efficiency and RPM calculation can be found in the main source by Royce et al. The compressor power is calculated via eq. (17).

$$W_a = P_1 Q_1 \frac{k}{\eta_a (k-1)} \left(r_p^{\frac{k-1}{k}} - 1 \right) \tag{17}$$

W_a … Compressor power in W
P_1 … Inlet pressure in Pa
k … Isentropic exponent in –
r_p … Pressure ratio between inlet and outlet in –
η_a … adiabatic efficiency in –

The diameter of the screw is sized by the required displacement volume in eq. (18).

$$Q_r = \frac{d^3 \left(\frac{L}{d}\right)}{C} \tag{18}$$

Q_r … Displacement volume in m³/min
d … Screw diameter in m
C … Screw profile constant (=2.055)
L/d … Ratio of screw length to diameter

Following, the area section of an existing Fairchild 'N' profile in Figure 8 is multiplied with the screw length and the density of steel to determine the mass of the screws via eq. (19).

$$m_{screw} = A_{profile} \cdot L \cdot \rho_{steel} \tag{19}$$

m_{screw} … Mass of the screws in kg
$A_{profile}$ … Screw profile area in m²

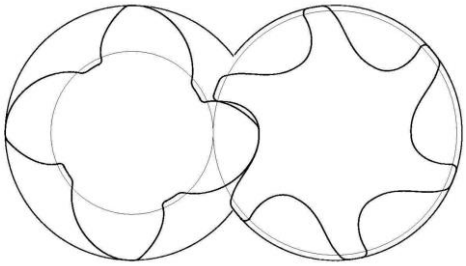

Figure 8: 'N' Screw Profile of a Fairchild aerospace compressor

The mass of the screw compressor is calculated by taking the volume of the screws and adding a 55% mass increase for the aluminium housing, which is a very rough estimation based on reviewing the housing design of an existing Fairchild screw compressor.

The compressor motor mass is selected in eq. (20) through the required compressor power considering an electric motor power density of 8kW/kg.

$$m_{compressor} = m_{screw} \cdot 1.55 + m_{motor} \tag{20}$$

m_{motor} … Mass of the compressor motor in kg

4.2.5. Model to consider mass increases due to increased power demand

While real snowball effects are not considered in this research, the following approach aims to give an indication of how additional power demands due to drag and electric power demands for the TMS increase the mass of the aircraft. The main source of required additional propulsive power is assumed to be the drag induced by the HX. This drag is then converted to power using the velocity of the aircraft. To derive the required shaft power, the power is multiplied with an assumed propulsive efficiency of the fan. Using power densities for the propulsion system, the fuel cell and the battery, the additional mass required to overcome the drag is calculated in eq. (21-22).

$$P_{drag} = F_{drag,HX} * v_a \tag{21}$$

$$P_{shaft} = \frac{P_{drag}}{\eta_{prop}} \quad (22)$$

$$m_{e,prop} = P_{shaft} \cdot \left(\frac{1}{\eta_{psys}} + \frac{PSC}{\eta_{FC}} + \frac{1 - PSC}{\eta_{Batt}} \right) \quad (23)$$

$m_{e,prop}$ … extra mass of the prop. Sys. In kg
P_{shaft} … shaft power in W
$\eta_{psys,FC,Batt,prop}$ efficiency of prop. Sys., battery, fuel cell as well as propulsive efficiency
P_{drag} … drag power in W
$F_{drag,HX}$ … drag force in N

Since the TMS has components that require a significant amount of electric power for operation – especially the TEC system, the additional mass for this power generation $m_{e,elec}$ is also considered by multiplying the sum of required electric power P_{elec} with the inverse power densities of both fuel cell and battery. Hydrogen storage is not considered here. The power is distributed according to the PSC (Power split) to FC and battery in eq. (24).

$$m_{e,elec} = P_{elec} \cdot \left(\frac{PSC}{\eta_{FC}} + \frac{1 - PSC}{\eta_{Batt}} \right) \quad (24)$$

Finally, the mass of the TMS m_{TMS} is summarized with the extra mass due to additional propulsive power and electric power in m_{total} eq. (25).

$$m_{total} = m_{e,prop} + m_{e,elec} + m_{TMS} \quad (25)$$

The analytical models and approach that are applied in this research are useful to investigate large parameter spaces with small computational time and provide realistic trends. To provide feasible results, the models for the compressor sizing and heat exchanger sizing have been compared to literature results and technical specifications of existing components in Annex-A. However, the results of this research should be interpreted as indications due to the low fidelity of the mass estimation models.

5. RESULTS

5.1. Architecture A1

Mass: The results for architecture A1 are shown in Figure 9 (top). For the chosen power class of the propulsion system, the TMS system mass varies between 150kg and 390kg depending on the power split. The lowest mass is achieved, when only the battery is used for Take-Off. However, this result only considers the Take-Off phase. The mass of the coolant is the main driver for TMS mass of A1. Coolant mass increases with the power split coefficient due to higher heat loads of the fuel cell. Corresponding to the coolant mass, the coolant pump mass also increases with the PSC and has a significant influence on the system mass. The TEC-system has a mass of between 0 and 40kg depending on the PSC and provides a lightweight option to raise the heat quality of the battery system so that heat can be rejected even on hot days. The mass of the heat exchanger is comparatively low at under 60kg for all cases.

Power consumption: Figure 10 (top) shows the power consumption of the TMS components: The TEC and the pump. It is visible, that the TEC power consumption dwarfs the power consumption of the coolant pump. At PSC=0.5, the TEC has a power consumption of 65kW.

Total: Figure 11 (top) shows however, that while the HX is comparatively light, the drag greatly increases the mass of the TMS, while the required power by the TEC leads to minor increased mass – especially at PSC>0.5. At a power split of 1, the additional mass is approximately twice as large as the mass of the thermal management system.

5.2. Architecture A2

Mass: Figure 9 (middle) shows the results of the mass calculation for architecture A2. The main drivers for the mass of A2 are the condenser, the coolant & refrigerant mass as well as the compressor. Similarly to A1 the coolant pump mass also has a significant influence on the total system mass. The TMS system mass rises from under 400kg to over 800kg and is around twice as heavy as A1. This comes as no surprise due to the number of additional components necessary for a VCS. The heat exchanger (condenser) on the air side of the system has a mass of around 30kg. The TMS mass of A2 rises roughly linearly with the PSC.

Power consumption: Figure 10 (middle) shows the power consumption of the TMS. In addition to the TEC power demand, power is required to operate the compressor of the VCS. The power demand of the compressor varies with the PSC, as there is higher heat load at higher PSCs from around 50kW to 250kW.

Total mass: Figure 11 (middle) shows that the additional mass from drag is reduced from 1150kg to 650kg. However, there is extra mass due to the power consumption of the VCS compressor which increases the total mass. In summary, at a PSC of 0.5 the VCS a mass of 1300kg yields a reduction of approx. 200kg compared to A1. Figure 12 shows, that when condensing temperature is varied, a condensing temperature of 160°C yields the lowest total mass for ranges between 120°C-240°C.

5.3. Architecture A3

Mass: Qualitatively, the results depicted in Figure 9 (bottom) have the same trends as Architecture A1. Due to the higher coolant temperature the HT-PEMFC needs a much smaller heat exchanger for the fuel cell. This leads to reduced drag compared to A1. Since the amount of coolant is related to the heat that needs to be rejected, the coolant mass does not change significantly from A1 to A3.

Power Consumption: A3 has the same battery heat flow that needs to be rejected via the TEC as A1. For this reason, the power consumption in Figure 10 (bottom) is identical to A1.

Total mass: Since the power consumption of A3 is identical to A1, the extra mass related to the power consumption of the TMS is also identical (see Figure 11 (bottom). The lower drag due to the smaller heat exchanger leads to a reduced total mass from drag. This effect is so pronounced that the total mass at a PSC of 0.5 is 550kg compared to A1 with 1500kg and A2 with 1300kg.

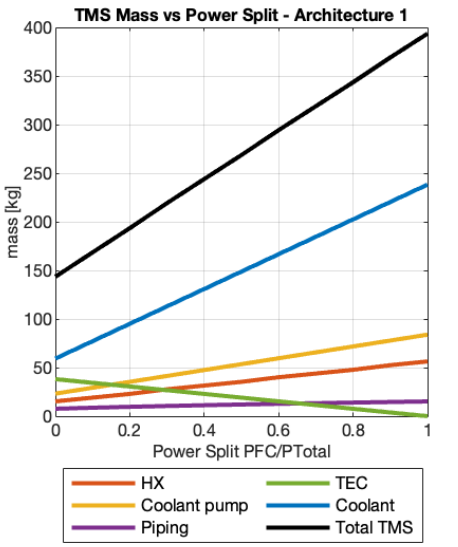

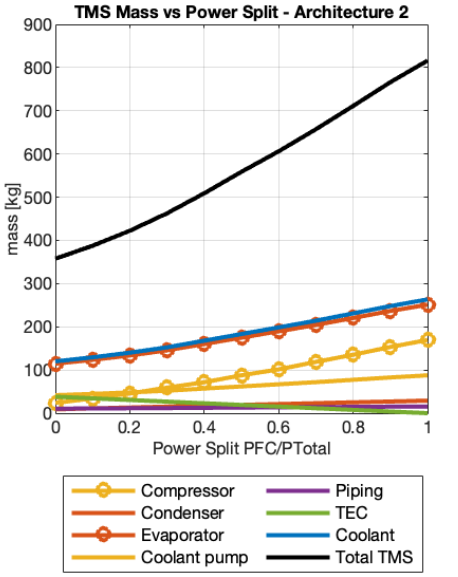

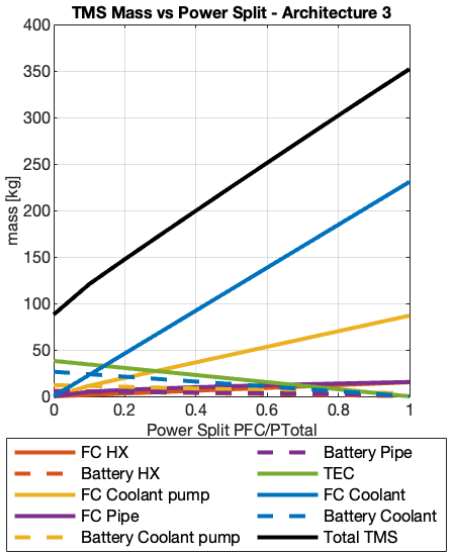

Figure 9: Mass of TMS vs. power split coefficient for Architectures A1 (top), A2 (middle) & A3 (bottom)

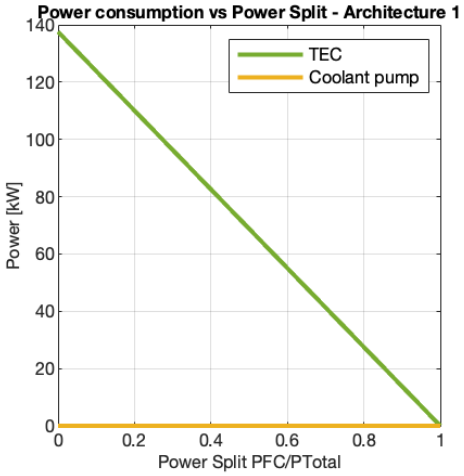

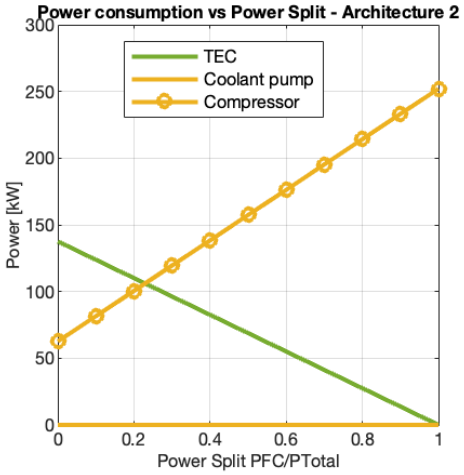

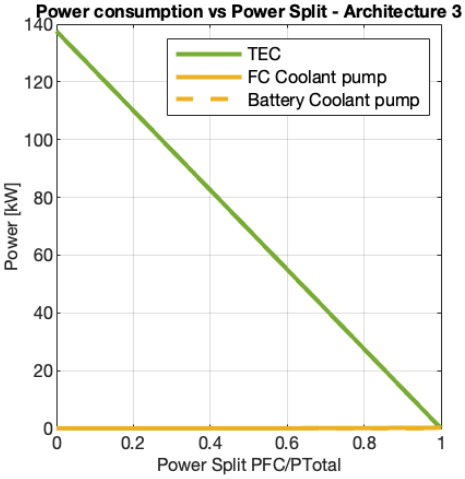

Figure 10: Power consumption of TMS components vs. power split coefficient for Architectures A1 (top), A2 (middle) & A3 (bottom)

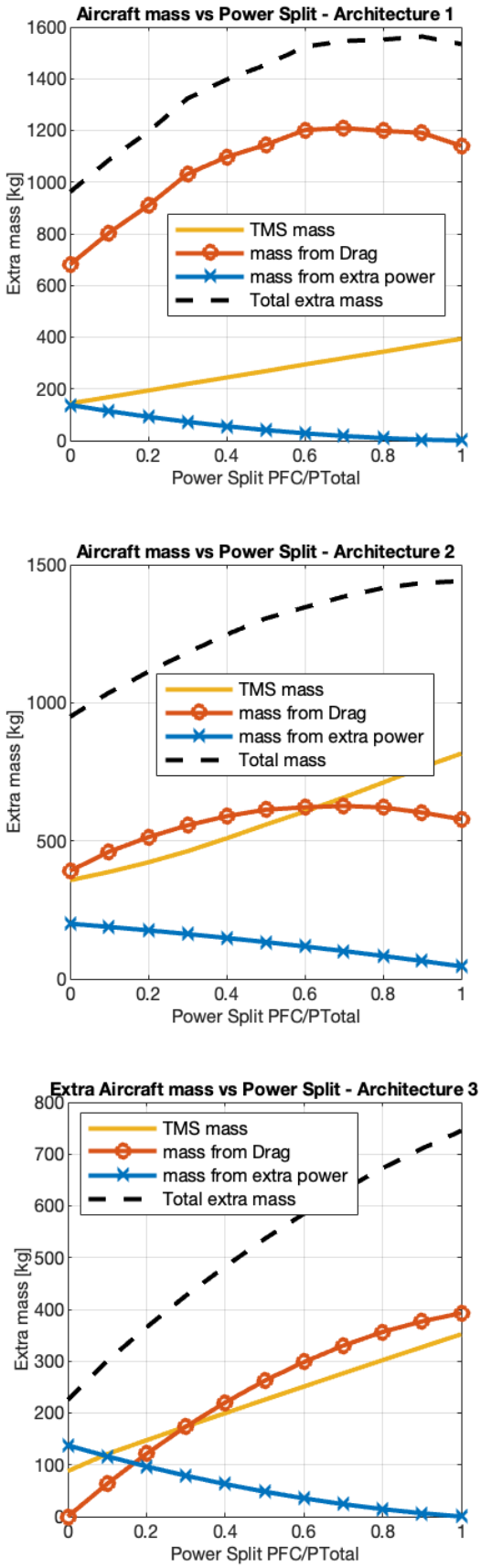

Figure 11: TMS mass, extra mass and total mass vs. power split coefficient for Architectures A1 (top), A2 (middle) & A3 (bottom)

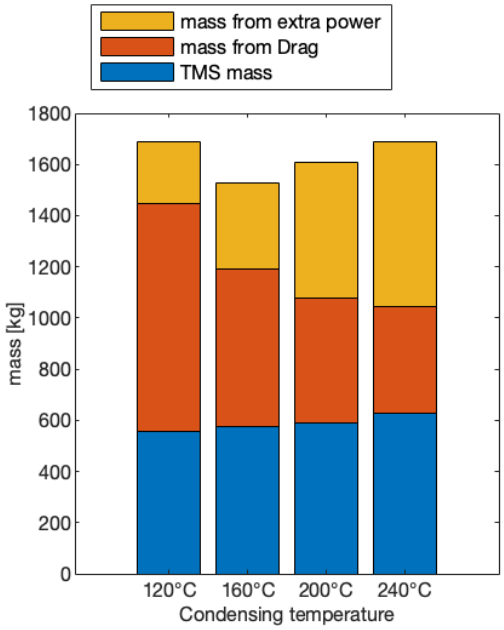

Figure 12: Total mass for different condensing temperatures of the VCS at a battery discharge rate of 1C.

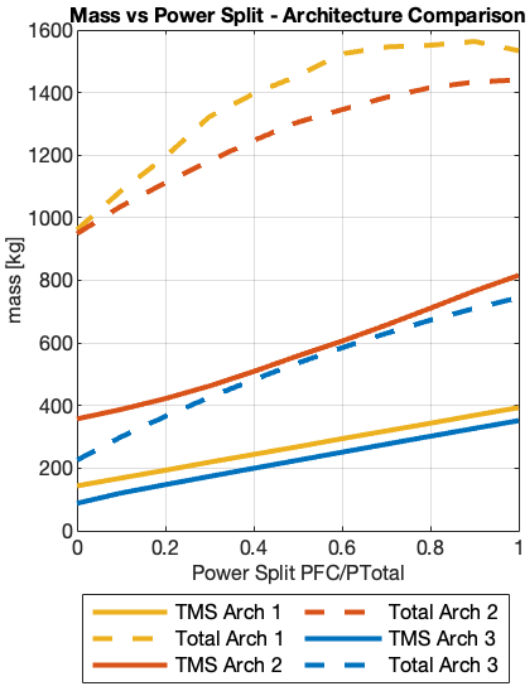

Figure 13: Comparison of total mass and TMS mass vs. power split for all Architectures

6. DISCUSSION

The comparative results show that there may be a benefit in using a VCS with water as a refrigerant to increase the heat quality of the described TMS when hot-day take-off is considered as the design point. With only 14% mass decrease between A1 and A2, this benefit is rather small considering the cost and complexity of installing, running and maintaining a VCS in an aircraft. Additionally, the benefit of the VCS becomes more questionable when the

design of the TMS is performed for a day with standard temperature and when the whole aircraft mission profile is considered. While in this research only a single-stage VCS was applied to raise the coolant temperature, cascading systems with different refrigerants may lead to further mass reductions compared to A1. The described VCS is based on available technology in industry and may be a short-term improvement for current fuel cell/battery electric aircraft development. However, the TRL of water as refrigerant is very low and would need to be increased. Water as refrigerant is non-combustible, non-toxic and has a good performance in high-temperature heat pumps. When water is used as a refrigerant, its low density in the gaseous state may be a driving factor for sizing the VCS components.

Much larger mass reductions have been shown in the results of this paper when using a HT-PEMFC without a VCS. Due to the high operating temperatures, the HX can be smaller than in A1 and therefore the additional mass due to the drag is greatly reduced. Additionally, power consumption is much lower due to the obsolete VCS compressor. An approximate 65% reduction in TMS mass is achieved compared to the reference A1. It must be mentioned that the HT-PEMFC technology is still in development and major hurdles need to be overcome to increase the TRL. This also means that the predictions for power density and operating temperature that are used here may be optimistic or not accurate for a future HT-PEMFC.

While this research has given an indication on the performance of TEC, VCS and HT-PEMFC when designing a system for the hot-day take-off as a design point, it is necessary to consider full mission profiles to design a TMS that is optimized for aircraft operation. Future research should consider also alternative methods that may be able to temporarily cool the fuel cell and battery system for take-off and climb. Such technologies could include phase change materials.

7. CONCLUSION

This research has investigated and compared three aircraft TMS-architectures for fuel cells and batteries related to their performance in terms of mass and power consumption during hot-day-take-off at ambient temperatures of 43.2°C.

The following conclusions can be drawn from the results of this research:

1. VCS may be a feasible way to improve hot-day take-off capabilities of fuel cell/battery aircraft in the short term. The results have shown that while the component mass and power consumption is increased with the VCS, the mass required to compensate for the HX drag is reduced. This has led to a 14% decrease in total mass (TMS component mass + mass required to overcome the HX drag and provide electric power to the TMS). The high TRL of VCS makes them an attractive option to improve the performance of LT-PEMFC TMS at high ambient temperatures. However, the TRL of high-temperature VCS is still low in aviation.

2. HT-PEMFC are able to reduce the total mass of the TMS by approx. 65% compared to the reference case using an LT-PEMFC. While the assumptions in this research may be optimistic, this shows the great potential that HT-PEMFC have to reduce fuel-cell TMS mass.

3. The drag induced by the TMS results in additional power demand on the propulsion and energy system. The TMS power demand also has to be provided by the energy system. When considering power densities of the propulsion and energy system, this has lead to an increase of system mass by a factor of 2-10 depending on the architecture.

8. ACKNOWLEDGEMENTS

This research was performed within the Horizon Europe project exFan. The authors would like to thank the research consortium of exFan. This research is funded by the European Union under GA No. 101138184. Views and opinions expressed are however those of the author(s) only and not necessarily reflect those of the European Union or CINEA. Neither the European Union nor CINEA can be held responsible for them.

9. REFERENCES

[1] W. Affonso *et al.*, ‘Thermal Management challenges for HEA – FUTPRINT 50’, *IOP Conf. Ser.: Mater. Sci. Eng.*, vol. 1024, no. 1, p. 012075, Jan. 2021, doi: 10.1088/1757-899X/1024/1/012075.

[2] ‘Micro Vapor Cycle System for Defense’. Accessed: Sep. 20, 2024. [Online]. Available: https://aerospace.honeywell.com/us/en/products-and-services/product/hardware-and-systems/air-and-thermal-systems/micro-vapor-cycle-system-for-defense

[3] ‘HONEYWELL AEROSPACE INVESTOR TECHNOLOGY TOUR.pdf’. Accessed: Sep. 20, 2024. [Online]. Available: https://static.seekingalpha.com/uploads/sa_presentations/903/89903/original.pdf

[4] ‘eVTOL Leaders Continue to Accelerate Progress’. Accessed: Sep. 20, 2024. [Online]. Available: https://evtol.news/news/evtol-leaders-continue-to-accelerate-progress

[5] M. Coutinho *et al.*, ‘A review on the recent developments in thermal management systems for hybrid-electric aircraft’, *Applied Thermal Engineering*, vol. 227, p. 120427, Mar. 2023, doi: 10.1016/j.applthermaleng.2023.120427.

[6] T. Kösters, X. Liu, D. Kozulovic, S. Wang, J. Friedrichs, and X. Gao, ‘Comparison of phase-change-heat-pump cooling and liquid cooling for PEM fuel cells for MW-level aviation propulsion’, *International Journal of Hydrogen Energy*, vol. 47, Aug. 2022, doi: 10.1016/j.ijhydene.2022.06.235.

[7] S. Maalouf, A. Isikveren, P. Dumoulin, N. Tauveron, and N. Cotereau, ‘High Temperature Heat Pump for

Aircraft Engine Oil Cooling', *Journal of Thermophysics and Heat Transfer*, pp. 1–11, Nov. 2018, doi: 10.2514/1.T5494.
[8] 'ARP85G: Air Conditioning Systems for Subsonic Airplanes - SAE International'. Accessed: Sep. 20, 2024. [Online]. Available: https://www.sae.org/standards/content/arp85g/
[9] H. J. Goldsmid, *Introduction to Thermoelectricity*, 2nd ed. 2016 Edition. Berlin Heidelberg: Springer, 2016.
[10] H. Kellermann, S. Fuhrmann, M. Shamiyeh, and M. Hornung, 'Design of a Battery Cooling System for Hybrid Electric Aircraft', *Journal of Propulsion and Power*, vol. 38, pp. 1–16, May 2022, doi: 10.2514/1.B38695.
[11] T. Hendricks, C. Tarau, and R. Dyson, 'Hybrid Electric Aircraft Thermal Management: Now, New Visions and Future Concepts and Formulation', Jun. 2021, pp. 467–476. doi: 10.1109/ITherm51669.2021.9503205.
[12] 'Clean Hydrogen JU - SRIA Key Performance Indicators (KPIs) - Clean Hydrogen Partnership'. Accessed: Sep. 20, 2024. [Online]. Available: https://www.clean-hydrogen.europa.eu/knowledge-management/strategy-map-and-key-performance-indicators/clean-hydrogen-ju-sria-key-performance-indicators-kpis_en
[13] S. Kazula, S. de Graaf, and L. Enghardt, 'Review of fuel cell technologies and evaluation of their potential and challenges for electrified propulsion systems in commercial aviation', *J. Glob. Power Propuls. Soc.*, vol. 7, pp. 43–57, Feb. 2023, doi: 10.33737/jgpps/158036.
[14] K. Barabanova, 'ZeroAvia High Temperature Fuel Cell Testing Shows Large Aircraft and Rotorcraft Potential for Hydrogen-Electric Propulsion', ZeroAvia. Accessed: Sep. 20, 2024. [Online]. Available: https://zeroavia.com/htpem-fuel-cell-testing/
[15] 'Next generation of improved High Temperature Membrane Electrode Assembly for Aviation | NIMPHEA Project | Fact Sheet | HORIZON', CORDIS | European Commission. Accessed: Sep. 20, 2024. [Online]. Available: https://cordis.europa.eu/project/id/101101407
[16] 'Future enabLing technologies for hYdrogen-powered Electrified aero engine for Clean aviatiOn | FlyECO Project | Fact Sheet | HORIZON', CORDIS | European Commission. Accessed: Sep. 20, 2024. [Online]. Available: https://cordis.europa.eu/project/id/101138488
[17] 'MIL-HDBK-310.pdf'. Accessed: Sep. 20, 2024. [Online]. Available: https://cvgstrategy.com/wp-content/uploads/2013/08/MIL-HDBK-310.pdf
[18] A. Stephan *et al.*, 'Alternative Battery Technologies Roadmap 2030+', 2023, Accessed: Sep. 20, 2024. [Online]. Available: https://publica.fraunhofer.de/handle/publica/451421
[19] 'Strategy', Aerospace Technology Institute. Accessed: Sep. 20, 2024. [Online]. Available: https://www.ati.org.uk/strategy/
[20] 'Performance Analysis and Optimization of a High-Temperature PEMFC Vehicle Based on Particle Swarm Optimization Algorithm'. Accessed: Sep. 20, 2024. [Online]. Available: https://www.mdpi.com/2077-0375/11/9/691
[21] ANTJE LINK and MARTIN STAGGAT, 'Characterisation of thermal management specific heat rejection for electric propulsion architectures', p. 14 pages, 2023, doi: 10.13009/EUCASS2023-262.
[22] P. Bachmann, V. Gümmer, and P. Polte, 'A Preliminary Design Method for Corrugated Louver Fin and Rectangular Offset Strip Fin Heat Exchangers', p. 14 pages, 2023, doi: 10.25967/570189.
[23] R. K. Shah and D. P. Sekulić, *Fundamentals of heat exchanger design*. Hoboken, NJ: Wiley, 2003.
[24] D. Saltzman *et al.*, 'Design and evaluation of an additively manufactured aircraft heat exchanger', *Applied Thermal Engineering*, vol. 138, Apr. 2018, doi: 10.1016/j.applthermaleng.2018.04.032.
[25] 'Screw compressor for water vapor heat pump technology.pdf'. Accessed: Sep. 20, 2024. [Online]. Available: https://heatpumpingtechnologies.org/annex58/wp-content/uploads/sites/70/2022/07/srmhthpannex58final.pdf
[26] T. Delash, 'Rotor Retrofit for Better Screw Compressor Performance in Refrigeration and Air Conditioning International Conference on Compressor Technology', Nov. 2012.
[27] R. N. Brown, *Compressors: Selection and Sizing*. Gulf Professional Publishing, 1997.
[28] 'specific-power.pdf'. Accessed: Sep. 20, 2024. [Online]. Available: https://www.hpccompressors.co.uk/media/159680/specific-power.pdf
[29] 'Rotrex-Technical-Datasheet-EK40-Rev1.9.pdf'. Accessed: Sep. 20, 2024. [Online]. Available: https://rotrex-fuel-cell-compressor.com/wp-content/uploads/2024/04/Rotrex-Technical-Datasheet-EK40-Rev1.9.pdf
[30] 'Rotrex-Technical-Datasheet-EK10-Rev2.4.pdf'. Accessed: Sep. 20, 2024. [Online]. Available: https://rotrex-fuel-cell-compressor.com/wp-content/uploads/2024/04/Rotrex-Technical-Datasheet-EK10-Rev2.4.pdf

10. ANNEX-A: MODEL VALIDATION

Some models used in this research have been adapted for different purposes and assumptions. To make sure that the assumptions have been chosen correctly, the models of the compressor and the heat exchanger are compared to testing results from literature below.

10.1. Compressor model validation

Comparison with 22kW VSD industrial screw compressors at a volume flow of 1.32m^3/min at 7.5bar. Table 3 shows, that the results in terms of specific power match up well with the shown industrial air compressors.

Table 3: Comparison of specific power with industrial screw compressors.

Model	Specific power [kW/(m3/min)]	Source
HPC ASD 50 SFC 22kW	6.44	[28]

Equivalent non-HPC compressor	7.5	[27]
Screw compressor model	7.5	Present model

Additionally, the model results were compared to centrifugal compressor systems by the company Rotrex. These systems are designed to be used in mobility applications for fuel cells and are thus sized for maximum power density. To achieve this comparison, the maximum air mass flow range and pressure ratio range were taken as an input to the present compressor model. Values for the Rotrex compressor specifications were taken from the respective datasheets. The results are shown in Table 4.

Table 4: Comparison of power density with fuel cell compressors for mobility applications

Model	**Power density [kW/kg]**	**Source**
Rotrex EK40C	1.22	[29]
Screw compressor model	0.82	present model
Rotrex EK10	1.13	[30]
Screw compressor model	1.01	present model

Power density of the screw compressor was generally lower compared to the Rotrex fuel cell compressors. However, this may be due to basing the comparison on the maximum mass flow range and the maximum pressure ratio which often do not coincide in real compressors. For the present research, the gap in power density was deemed acceptable.

10.2. Heat exchanger model validation

The present analytical heat exchanger model was compared with results from Saltzman et al.[24] to validate its use for aviation heat exchangers. The geometry data and operating conditions given in Saltzman were applied to the present model. The model displays the measured behaviour of Saltzman with little deviation.

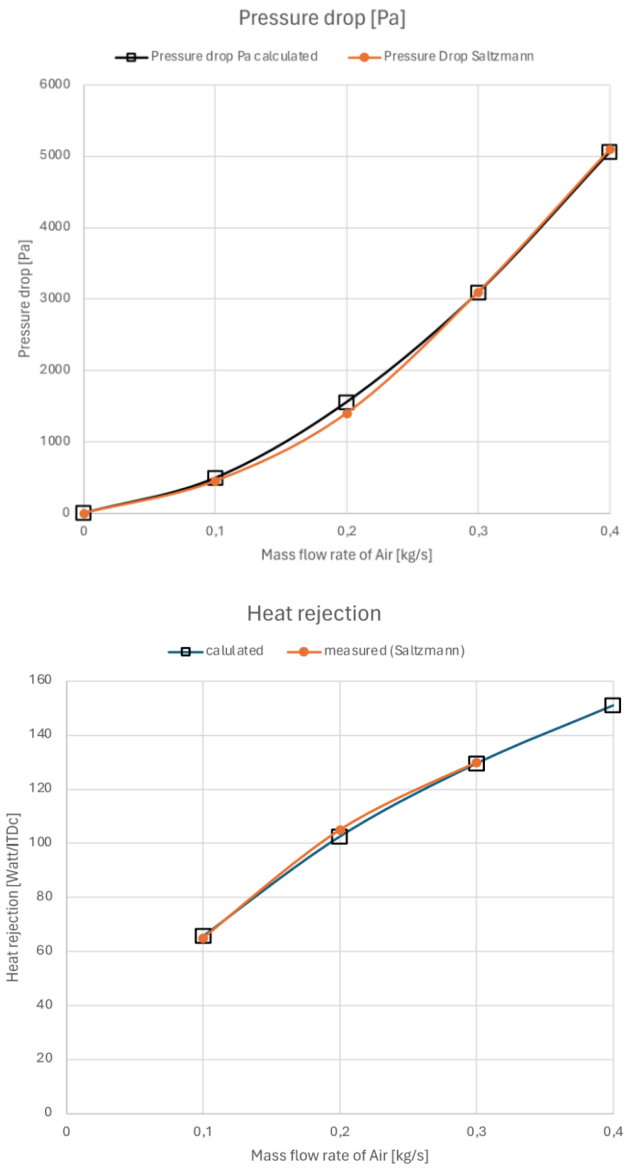

Figure 14: Comparison of present HX model with literature testing results regarding pressure drop and heat rejection